

# Hierarchical Assembly of Plasmonic Nanoparticle Heterodimer Arrays with Tunable Sub-5 nm Nanogaps

Jiajing Li,<sup>†</sup> Tian-Song Deng,<sup>‡,§</sup> Xiaoying Liu,<sup>†</sup> James A. Dolan,<sup>†,||,⊥</sup> Norbert F. Scherer,<sup>‡,§</sup> and Paul F. Nealey<sup>\*,†,||,⊥</sup>

<sup>†</sup>Pritzker School of Molecular Engineering, University of Chicago, Chicago, Illinois 60637, United States

<sup>‡</sup>The James Franck Institute, University of Chicago, Chicago, Illinois 60637, United States

<sup>§</sup>Department of Chemistry, University of Chicago, Chicago, Illinois 60637, United States

<sup>||</sup>Material Science Division, Argonne National Laboratory, Lemont, Illinois 60439, United States

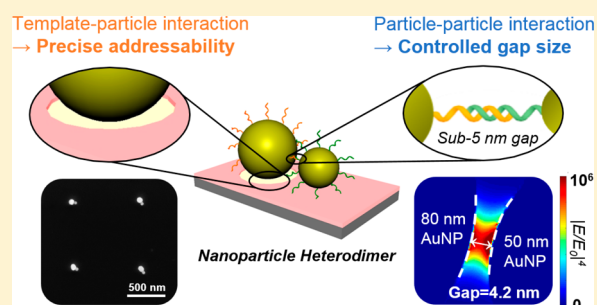
<sup>⊥</sup>The Institute for Molecular Engineering, Argonne National Laboratory, Lemont, Illinois 60439, United States

## Supporting Information

**ABSTRACT:** Nanoparticle assemblies have generated intense interest because of their novel optical, electronic, and magnetic properties that open up numerous opportunities in fundamental and applied nanophotonics, -electronics, and -magnetics. However, despite the great scientific and technological potential of these structures, it remains an outstanding challenge to reliably fabricate such assemblies with both nanometer-level structural control and precise spatial arrangements on a macroscopic scale. It is the combination of these two features that is key to realizing nanoparticle assemblies' potential, particular for device applications.

To address this challenge, we propose a hierarchical assembly approach consisting of both template–particle and particle–particle interactions, whereby the former ensures precise addressability of assemblies on a surface and the latter provides nanometer-level structural control. Template–particle interactions are harnessed via chemical-pattern-directed assembly, and the particle–particle interactions are controlled using DNA-directed self-assembly. To demonstrate the potential of this hierarchical assembly approach, we demonstrate the fabrication of a particularly fascinating assembly: the nanoparticle heterodimer, which possesses a surprisingly rich set of plasmonic properties and is a promising candidate to enable a variety of imaging and sensing applications. Each heterodimer is placed on the surface at predetermined locations, and the precise control of the nanogaps is confirmed by far-field scattering measurements of individual dimers. We further demonstrate that the gap size can be effectively tuned by varying the DNA length. By correlating measured spectra with finite-difference time-domain (FDTD) simulations, we determine the gap sizes to be 4.2 and 5.0 nm—with subnm deviation—for the two DNA lengths investigated. This is one of the best gap uniformities ever demonstrated for surface-bound nanoparticle assemblies. The estimated surface-enhanced Raman scattering (SERS) enhancement factor of these heterodimers is on the order of  $10^5$ – $10^6$  with high reproducibility and predictable polarization-dependence. This hierarchical fabrication technique—employing both template–particle and particle–particle interactions—constitutes a novel platform for the realization of functional nanoparticle assemblies on surfaces and thereby creates new opportunities to implement these structures in a variety of applications.

**KEYWORDS:** hierarchical assembly, DNA, heterodimers, nanophotonics



## INTRODUCTION

Designing and fabricating functional nanostructures from individual nanoparticle (NP) building blocks is both a foundational activity and an enduring challenge for the nanoscience and -technology communities. The ability to successfully and reliably exploit the properties of these structures depends sensitively on the control we can exert upon their morphology and spatial arrangement. Morphological control depends largely upon mediating the thermodynamic interactions between individual building blocks (i.e., particle–particle interactions), whereas modulating the interactions between NPs and surfaces (i.e., template–particle

interactions) is crucial to achieving a controlled and predetermined spatial arrangement of assemblies. Common fabrication approaches rely on only one or the other of these two types of interactions. Nanostructures assembled in solution utilize interactions between low-cost single-crystal colloidal NPs with tailored composition, size, and shape,<sup>1,2</sup> which allows for well-controlled properties of these assemblies. The interparticle spacing of dimers in solution, for example,

**Received:** February 22, 2019

**Revised:** May 22, 2019

**Published:** June 11, 2019

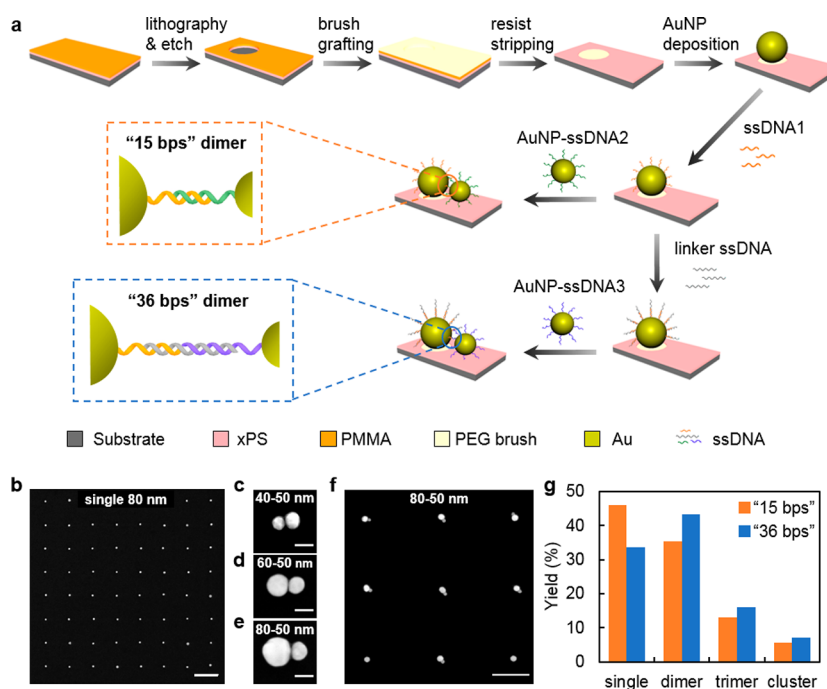


**Figure 1.** Fabrication of AuNP heterodimer arrays. (a) Schematic of the hierarchical assembly of AuNP heterodimers. Following electron beam lithography and oxygen plasma etching, the PEG brush is selectively grafted to the substrate within the lithographically patterned areas; the unpatterned areas are protected by xPS. Single AuNPs are selectively immobilized on the patterned areas due to hydrogen bonding between the citrate-capped AuNPs and the PEG brush. (b) The yield of single-AuNP arrays is essentially 100%. Single-AuNP arrays are then functionalized with ssDNA1. To construct heterodimers, AuNP conjugates functionalized with complementary ssDNA2 then hybridize with the ssDNA1-functionalized AuNPs, bringing the ssDNA2-functionalized AuNPs to an adjacent position. Alternatively, linker ssDNA can be added between the two particles to further alter the length of the hybridized DNA. The hybridized DNA is 15 bps and 36 bps long for heterodimers assembled without and with linker ssDNA, respectively. Larger interparticle spacing is expected for “36 bps” dimers as a result of the longer DNA length. (c)–(e) Heterodimers of 40–50, 60–50, and 80–50 nm sizes can be readily assembled following the hierarchical approach. (g) Dominant structures after assembly are heterodimers and single AuNPs. Scale bars: (b), (f) 500 nm; (c), (d), (e) 50 nm.

can easily reach sub-5 nm which, coupled with the tremendous field enhancement in the gap, enables single-molecule level detection.<sup>3–5</sup> However, a reliable way to transfer the assembled structures from solution to a surface with full addressability and minimal structural alterations remains elusive, thereby limiting the technological usefulness of such solution-processed structures. On the other hand, a few approaches have been developed to assemble functional nanostructures on lithographically defined patterns combined with chemical contrast, topographical contrast, and DNA origami,<sup>6–11</sup> enabling the controlled spatial arrangement and addressability of assemblies on a macroscopic length scale. However, in these cases, control over the uniformity and reproducibility of the structures (e.g., the interparticle spacing) is usually insufficient because of the lack of control over interparticle interactions. Consequently, an assembly approach that harnesses both template–particle and particle–particle interactions would represent a considerable advance in nanofabrication and enable access to structures that are otherwise near-inaccessible.

To answer this challenge, we demonstrate a hierarchical assembly approach consisting of chemical-pattern-directed assembly and DNA-directed self-assembly; the former provides control over template–particle interactions and the latter provides control over particle–particle interactions. To demonstrate this robust assembly approach, we fabricate a particularly interesting nanostructure, the nanoparticle heterodimer—two metallic nanoparticles differing in size in close proximity to one another. The surface plasmon resonances of the two nanoparticles can mix and hybridize analogously to

molecular orbitals in diatomic molecules.<sup>12,13</sup> This results in a surprisingly rich set of plasmonic properties for such a simple structure, such as electromagnetic field enhancement,<sup>14–16</sup> Fano resonances,<sup>17–19</sup> and the “optical nanodiode” effect,<sup>20,21</sup> enabling a wide range of potential applications. Despite the great potential of such heterostructures, they are still restricted in applications because of the lack of facile and robust assembly approaches.

Our hierarchical approach comprises two main steps: (1) the fabrication of single-nanoparticle arrays as “seeds” via chemical-pattern-directed assembly and (2) the “growth” of heterodimers from these seeds via DNA-directed self-assembly. The first step provides addressability for each nanostructure, and the second step offers tunable control of the interparticle spacing. The precise placement of each heterodimer enables straightforward optical characterization of individual structures and, therefore, statistical analysis of multiple structures, which in turn enables the determination of the distribution of gap size in combination with FDTD simulations. By comparing heterodimers formed with and without DNA, as well as heterodimers with different DNA lengths, we confirm the essential role of DNA in controlling the gap size. Far-field scattering and surface-enhanced Raman scattering (SERS) measurements of individual heterodimers further reveal their strong plasmonic coupling and potential as robust SERS-active nanostructures. This versatile assembly process, with precise addressability of individual nanostructures on a macroscopic scale and well-controlled structural properties, provides a

valuable platform for high-throughput nanomaterials for both fundamental exploration and device implementation.

## RESULTS

The fabrication scheme for gold nanoparticle (AuNP) heterodimer arrays is shown in Figure 1a. Fabrication begins with the positioning of single AuNPs on lithographically patterned substrates via a chemical-pattern-directed assembly. The substrate is first coated with cross-linked polystyrene (xPS) and poly(methyl methacrylate) (PMMA) resist, followed by electron beam lithography and oxygen plasma etching to create the desired patterns. The exposed substrate within the patterned areas is functionalized with hydroxyl-terminated poly(ethylene glycol) methyl ethers (PEG), and the unpatterned areas are protected by both the PMMA resist and xPS mat. After PMMA and excess PEG brush are removed, AuNPs are selectively immobilized within the patterned areas and form single-AuNP arrays with essentially 100% yield (Figure 1b), since the citrate ligands of AuNPs can form hydrogen bonds with the PEG, whereas the xPS mat provides only minimal adhesion.

To form heterodimer arrays, single-AuNP arrays are functionalized with thiolated single-strand DNA1 (ssDNA1) through a thiol attachment process modified from previously reported methods.<sup>22,23</sup> The ssDNA1 can hybridize with the single-strand DNA2 (ssDNA2)-functionalized AuNP conjugate and bring it adjacent to the immobilized single AuNP. The ssDNA1 and ssDNA2 are complementary; their sequence can be found in the Supporting Information. In this experiment, the hybridized double strand DNA (dsDNA) has 15 base pairs (bps), and the assembled dimer is referred to as the “15 bps” dimer. Alternatively, linker ssDNA can be added to increase the length of the hybridized dsDNA to 36 bps, and the dimer assembled with linker is correspondingly referred to as the “36 bps” dimer.

This flexible hierarchical assembly strategy can be readily applied to fabricate heterodimers of various sizes, as shown in Figure 1c–e. Indeed, AuNPs with diameters of 40, 60, and 80 nm are all observed to form heterodimers with 50 nm AuNP–DNA conjugates. This fabrication strategy therefore possesses clear advantages over other dimer fabrication methods, many of which require major modifications to the procedure when altering constituent particle size or shape. For example, dimers assembled on DNA origami templates would require different DNA structures to assemble particles of different sizes and shapes, which would be time-consuming and costly to implement. Clearly, the hierarchical assembly strategy demonstrated here requires no such modifications, and heterodimers of different sizes and shapes can be readily fabricated with little if any alteration to the established procedure.

We choose 80–50 nm dimers for further characterization (Figure 1f), as larger particles present fewer metrology challenges while still exhibiting similar plasmonic behavior to smaller particle heterodimers. After primary optimization of the DNA hybridization conditions (e.g., salt concentration and hybridization time), the yield of “15 bps” dimers is estimated to be 35% (based on the analysis of approximately two hundred assemblies), compared with 43% for “36 bps” dimers (Figure 1g). We anticipate the higher yield of “36 bps” dimers results from the reduced steric hindrance between the two constituent particles during hybridization. Since dsDNA is much more rigid than ssDNA,<sup>24</sup> after ssDNA1 hybridizes with

linker DNA, the hybridized dsDNA is less likely to adhere to the particle surface and increases the distance between the particle surface and the dangling end used for hybridization. As a result, the steric hindrance between the two particles is reduced, which facilitates subsequent hybridization with AuNP–ssDNA3 conjugates. Single nanoparticles are the predominant nanostructures besides dimers. However, they can be readily distinguished from dimers and excluded from subsequent analysis because of their distinctive optical response. We characterize the fabricated heterodimers by collecting their far-field light scattering and SERS spectra, which are very sensitive to the gap size.<sup>25,26</sup>

In order to characterize the gap sizes of nanoparticle heterodimers, we measure the longitudinal plasmon resonance of individual nanostructures. When incident light is polarized along the dimer axis, coupling of the two single-AuNP plasmonic resonances results in a strong red-shift of the resulting dimer longitudinal plasmon resonance. This red-shifted scattering peak is very sensitive to the heterodimer gap size. As a result, a narrow distribution of longitudinal plasmon resonance peak positions is anticipated for a population of heterodimers with well-controlled gap sizes. The dependence of the longitudinal plasmon resonance on gap size can be interpreted using a simple dipole–dipole interaction model.<sup>27</sup> For a single nanoparticle, polarized incident light induces an oscillating distribution of electrons within the particle that is phase shifted with respect to the incident field. However, when another particle is nearby (i.e., the case of a heterodimer) and the light is polarized along the dimer axis, the coupling of the two particles leads to a lower resonance frequency (red shift). As the gap size decreases and the coupling effect becomes stronger, the longitudinal plasmon resonance peak will become further red-shifted.<sup>28</sup> Under perpendicular polarization, on the other hand, the coulombic forces would be enhanced by the coupling, resulting in a slightly blue-shifted peak, the transverse plasmon resonance peak. This peak is relatively insensitive to the gap size and thus is not the focus of our analysis. The far-field scattering spectra of AuNP nanostructures are measured using a custom-built setup with spatially coherent white laser, a schematic of which is shown in Figure S1.

We first measure the scattering spectra of 80 nm diameter single AuNPs functionalized with ssDNA1. Three representative spectra are shown in Figure 2b (green solid lines), which agree well with the corresponding simulated spectrum (green dashed line). All spectra are normalized with respect to their maximum intensity for better comparison. The peak position is identified for each measured spectrum and their distribution is shown in Figure 2c. The distribution of peak positions is approximately normal (Gaussian) with a mean of 561 nm. We also measured the spectra before ssDNA functionalization in order to examine the impact of ssDNA on the optical properties of AuNPs. In this case, the distribution of peak positions is again approximately normally distributed with a mean of 562 nm. The 1 nm difference between the means of the two distributions is clearly within the standard error of the mean— $SD/\sqrt{N}$ , where SD is the standard deviation of peak positions, and  $N$  is the number of structures measured. This small difference is therefore more likely to result from statistical noise rather than any underlying difference between the two distributions. This result confirms that ssDNA functionalization only has a minimal, if any, impact on the optical properties of the AuNPs. This is not surprising since ssDNA has a refractive index ( $n = 1.5–1.6$ )<sup>29</sup> close to that of

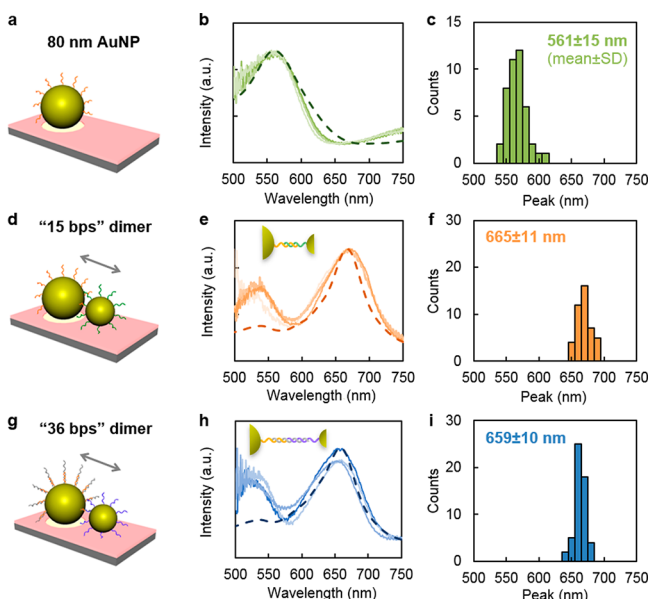


**Figure 2.** Scattering spectra of 80 nm single AuNPs and 80–50 nm heterodimers. (a) Schematic of 80 nm AuNP on the PEG functionalized substrate. (b) Experimentally measured scattering spectra (green solid lines) of 80 nm AuNPs are in good agreement with the simulated spectrum (green dashed line). (c) Experimental distribution of peak positions has a mean of 561 nm and a standard deviation of 15 nm. Scattering spectra of (d) “15 bps” dimers and (g) “36 bps” dimers are measured with incident light polarized along the dimer axis. Representative spectra are shown in (e) and (h) with good reproducibility. The gap size of simulated heterodimers is varied to obtain the best fit between simulated and measured spectra. (f) “15 bps” dimers exhibit a mean peak position of  $665 \pm 11$  nm, and (i) “36 bps” dimers exhibit a less red-shifted mean value of  $659 \pm 10$  nm as obtained from the experimental data.

the immersion oil ( $n = 1.515$  at 546 nm) used in these measurements.

Individual heterodimers were characterized with incident light polarized along the dimer axis (Figure 2d, 2g). Representative spectra are shown in Figure 2e and Figure 2h. The right peak comes from the longitudinal plasmon resonance, whereas the left peak arises from the transverse mode, which arises as the incident light is not perfectly parallel with the dimer axis during measurement. We focus only on the longitudinal plasmon resonance peak in our analysis. Clearly, the longitudinal plasmon resonance is strongly red-shifted compared with the localized surface plasmon resonance of single AuNPs. For “15 bps” dimers, the mean of the experimental distribution of peak positions occurs at 665 nm (Figure 2f). For “36 bps” dimers, the DNA linking the two particles is longer, and the resulting mean therefore exhibits a smaller red-shift, occurring at 659 nm (Figure 2i). We conducted a Welch’s  $t$  test<sup>30</sup> in MATLAB to examine if the two distributions of peak positions are significantly different from one another. The test confirms their difference at the 5% significance level. Therefore, the difference in mean peak positions (most likely) arises from a different gap size rather than measurement noise.

In order to estimate the mean gap size—and its likely distribution—from the measured longitudinal plasmon peaks, we calculate the longitudinal resonances of 80–50 nm dimers with various gap sizes using FDTD simulations (Figure 3a,b). Although the fractional plasmon wavelength shift decays

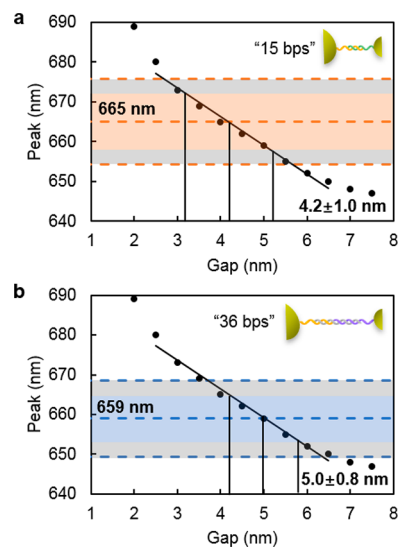


**Figure 3.** Estimation of mean gap size and gap size distribution. Longitudinal plasmon peaks of 80–50 nm dimers with various gap sizes are calculated using FDTD simulations. The dependence of peak position on gap size is approximately linear in the range of measured peak distribution. Experimentally measured mean and standard deviation of the peak distributions are marked by dashed lines. The (a) orange and (b) blue shaded areas indicate the variation in peak distribution attributed to variation in gap size, and the gray shaded areas indicate the variation in peak distribution resulted from variation in particle size. The estimated gap size is  $4.2 \pm 1.0$  nm for “15 bps” dimer and  $5.0 \pm 0.8$  nm for “36 bps” dimer.

exponentially with gap size,<sup>31</sup> the longitudinal plasmon peaks depend approximately linearly on gap size over the narrow distribution of wavelengths measured. Assuming that all variation in the longitudinal plasmon peak positions arises from a variation in gap size, we estimate from the linear fit that the gap size for “15 bps” dimers is  $4.2 \pm 1.5$  nm and that for “36 bps” dimers is  $5.0 \pm 1.3$  nm, which is comparable with previously reported gap size induced by similar length of DNA in a dried state.<sup>3</sup> However, these variations in gap size are necessarily an overestimate as we are ignoring any impact of variation of particle size and shape. Therefore, for a more accurate estimate, we need to disentangle the impact of particle size and shape from that of gap size. As the impact of particle shape is challenging to simulate, we assume perfectly spherical nanoparticles and examine only the impact of particle size, for which the standard deviation (8%) is provided by the manufacturer.

We conducted a series of simulations to calculate longitudinal plasmon resonances at various gap size for different dimer radius (sum of individual particle diameters), and we obtained an expression for the peak position as a function of gap size and dimer diameter. The impact of particle size and gap size on the peak distribution can be disentangled using this function and error propagation rules, and the standard deviation of gap size can be calculated. (A detailed calculation procedure is provided in the [Supporting Information](#).) Using this procedure, the variation in gap size is found to be significantly smaller than that estimated when ignoring the effect of particle size: the estimated gap size is  $4.2 \pm 1.0$  nm for “15 bps” dimers and  $5.0 \pm 0.8$  nm for “36 bps” dimers, confirming the excellent control over gap distribution using the hierarchical assembly. However, this is again an overestimate of the variation in gap size, as the impact of

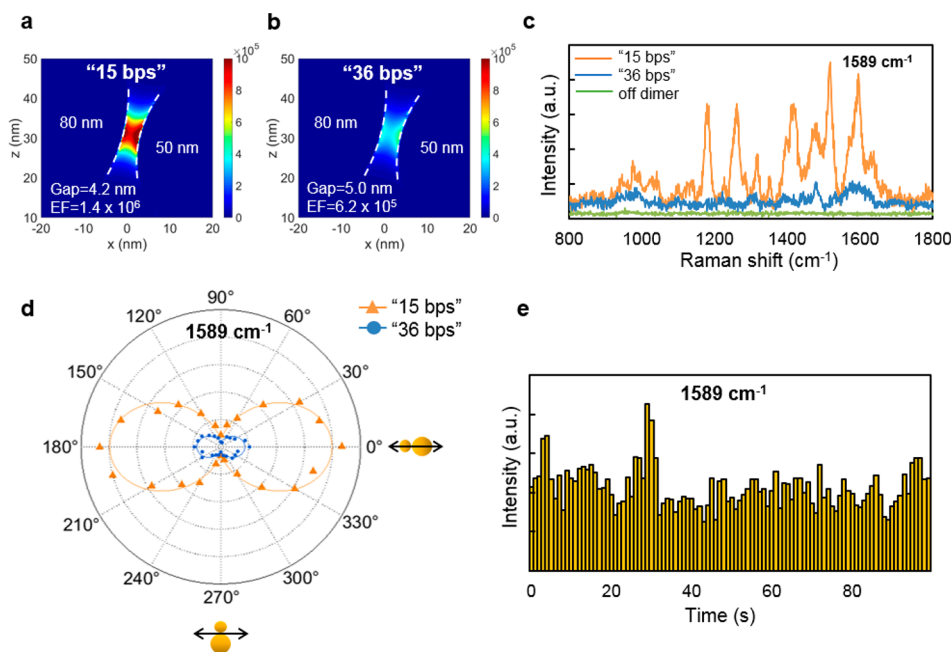


**Figure 4.** SERS measurements of 80–50 nm heterodimers. Simulated SERS enhancement factor of (a) the “15 bps” dimer is approximately  $1.4 \times 10^6$  and that of (b) the “36 bps” dimer is  $6.2 \times 10^5$ . (c) Both heterodimers show enhanced Raman signals of analytes, while no signal is observed from areas away from the dimers (“off dimer”). (d) Polar plots of average SERS intensities taken from five dimers exhibit a strong  $\cos^2\theta$  dependence. (e) Time-resolved SERS intensities at  $1589 \text{ cm}^{-1}$  (accumulation time 1 s, 100 measurements) remain stable over time.

particle shape has been ignored. Therefore, we estimate that the true standard deviation of the gap size should lie in the subnm regime.

To further confirm the essential role of particle–particle interaction in controlling the gap size, we compare heterodimers formed with and without DNA. The hierarchical assembly approach, as already demonstrated in this paper, employs both template–particle interaction and particle–particle interaction (e.g., DNA hybridization). Single nanoparticles are immobilized on a template substrate via chemical-pattern-directed assembly, followed by formation of heterodimers via DNA hybridization; the gap size is controlled by the length of the DNA. Alternatively, we can also construct heterodimers based solely on chemical-pattern-directed assembly without DNA (Figure S3a). Two adjacent patterned spots of different sizes are functionalized with the PEG brush, while the unpatterned areas are protected, as before, with xPS. The larger particle is first immobilized on the larger area, as the smaller area cannot provide sufficient adhesion to immobilize the larger particle. The smaller particle is then immobilized on the smaller area, forming a heterodimer. The interparticle spacing of such heterodimers, however, is much less controlled, and the dimers exhibit a far greater variety of far-field scattering spectra than those fabricated with DNA. For example, the two particles can be too distant—and, therefore, behave optically like two single AuNPs (Figure S3b)—or can be in extremely close proximity such that the coupled longitudinal plasmon resonance shifts toward the infrared (Figure S3d). The long-wavelength longitudinal plasmon scattering peaks of coupled heterodimers span the 700 to 900 nm range (Figure S3e), which is a much broader distribution of peak positions than that obtained with DNA (Figure 2f,i). The comparison with this control experiment confirms that the interparticle interactions, such as DNA hybridization, are key to controlling the gap size and optical properties of heterodimers.

Following characterization of heterodimers by far-field scattering, we examine their potential as SERS substrates. We first calculate the SERS enhancement factor (EF) of dimers using the gap size previously estimated. The EF is defined as  $(E/E_0)^4$ ,<sup>4</sup> where  $E$  is the local maximum electric field within the heterodimer gap and  $E_0$  is the amplitude of the source electric field. For “15 bps” dimers, the estimated gap size is 4.2 nm, and the EF is estimated from FDTD simulations to be  $1.4 \times 10^6$  (Figure 4a). For the “36 bps” dimer with a 5.0 nm gap, the EF is expected to be  $6.2 \times 10^5$  (Figure 4b). Note that the two particles here are not horizontally aligned, such that the incident electric field vector may be decomposed into two orthogonal components, parallel and perpendicular to the dimer center-to-center axis. It is the parallel component which contributes to the SERS enhancement; the perpendicular component has a minimal effect. We therefore expect the resulting height difference leads to a slightly lower EF when calculated with respect to the (horizontally aligned) incident electric field as the parallel component of the incident field is necessarily smaller than the total electric field ( $E_0$ ).

We conducted SERS measurements on assembled 80–50 nm heterodimers and compared the experimental results with simulations. The ssDNA1 is modified with Cy5 dye to better observe the SERS signals, and a 633 nm excitation wavelength is selected as it is resonant with Cy5.<sup>32</sup> A relatively low laser power ( $77.5 \mu\text{W}$ ) is employed to prevent laser-induced damage to the heterodimers. Repeated acquisition of SERS spectra from the same “15 bps” dimer demonstrates good reproducibility and reveals that there is no significant degradation caused by the laser over time (Figure 4e). In order to make a more quantitative comparison, we plotted the averaged Raman intensities of five heterodimers at  $1589 \text{ cm}^{-1}$  (a characteristic peak of Cy5<sup>33</sup>) for “15 bps” and “36 bps” dimers with the incident laser polarization rotated from 0 to  $360^\circ$  with respect to the dimer axis (Figure 4d). When the

incident laser is polarized parallel with the dimer axis, the EF of “15 bps” dimers is approximately 4.7 times greater than that of “36 bps” dimers. This finding is larger than that predicted by simulations. We expect this discrepancy to mainly arise from the different positions the dye molecules adopt in the two types of dimers. Dye molecules are attached to the termini of the ssDNA1 molecules away from the 80 nm AuNPs. For “15 bps” dimers, ssDNA1 directly hybridizes with 50 nm AuNP-ssDNA2 and the dye molecules are close to the surface of the 50 nm AuNPs. For “36 bps” dimers, however, ssDNA1 hybridizes with linker ssDNA before hybridizing with AuNP-ssDNA3, leaving the dye molecules near the center of the gap. A previous study revealed that the local SERS enhancement at the gap center is smaller than that close to the particle surface,<sup>16</sup> an effect that can lead to further exaggerated difference in the EF of the two dimers. A more detailed comparison at different polarization angles ( $\theta$ ) is shown in Figure S4, where the “15 bps” dimers show higher enhancement than that of the “36 bps” dimers at each polarization angle. The polarization-dependent SERS intensities is well fitted by  $\cos^2\theta$  curves, strongly corroborating the hypothesis that the dominant contribution to the SERS signal is the enhanced electromagnetic field arising from the coupled longitudinal plasmon resonance.<sup>34</sup>

## CONCLUSIONS

We have demonstrated a hierarchical assembly approach, combining chemical-pattern-directed assembly and DNA-directed self-assembly, to fabricate AuNP heterodimer arrays with controlled and tunable sub-5 nm gaps on a macroscopic scale. The precise placement of heterodimers on the functionalized surface enables optical characterization of individual nanostructures, as well as statistical analysis of multiple structures. Far-field scattering of assembled heterodimers reveals strong plasmonic coupling and a distinct red-shift of the longitudinal plasmon resonance compared with single AuNPs. By analyzing scattering spectra and FDTD simulations, we have confirmed that the interparticle spacing is indeed controlled by interparticle interaction, and we have estimated the gap size to be 4.2 and 5.0 nm for the “15 bps” and “36 bps” dimers investigated, respectively. We have also examined the variation of gap size and revealed that the distribution of longitudinal plasmon peaks can be largely attributed to the variation of particle size, while the gap size only has minimal, subnm variation. SERS measurements reveal a strongly enhanced electromagnetic field within the heterodimer gap resulting from the coupled plasmon resonance, and the estimated EF is on the order of  $10^5$ – $10^6$ , making the AuNP heterodimer arrays excellent SERS-active nanostructures.

This versatile assembly process has been demonstrated on both silicon wafer and conductive oxide-coated glass and is expected to be applicable to a wide variety of additional substrates. Furthermore, as this is a post-functionalization approach, where DNA functionalization takes place after the chemical-pattern-directed assembly, we anticipate that this assembly approach can also be extended to take advantage of other interparticle interactions, such as electrostatic attraction<sup>35</sup> and molecular linkers,<sup>5,36</sup> and could therefore be used to construct even more complex nanostructures (e.g., core-satellite<sup>37</sup> and Au–Ag heterostructures).<sup>38</sup> Nanostructure arrays fabricated from this approach, with nanometer-level structural control and precise addressability, hold great

potential for various applications including biosensors,<sup>39,40</sup> photocatalysis,<sup>41–43</sup> and optical information processing.<sup>44</sup>

## ASSOCIATED CONTENT

### Supporting Information

The Supporting Information is available free of charge on the ACS Publications website at DOI: 10.1021/acs.nanolett.9b00792.

Further information on experimental methods, characterization, and modeling; calculation of distribution of gap size; supplementary figures (PDF)

## AUTHOR INFORMATION

### Corresponding Author

\*E-mail: nealey@uchicago.edu.

### ORCID

Paul F. Nealey: 0000-0003-3889-142X

### Notes

The authors declare no competing financial interest.

## ACKNOWLEDGMENTS

This work was primarily supported by the U.S. Department of Energy, Basic Energy Sciences, Materials Sciences and Engineering Division. T.-S.D. and N.F.S. acknowledge support from the Vannevar Bush Faculty Fellowship program sponsored by the Basic Research Office of the Assistant Secretary of Defense for Research and Engineering and funded by the Office of Naval Research through grant N00014-16-1-2502 for the far-field light scattering experiments. SEM characterization and Raman scattering were carried out at NSF MRSEC shared user facilities at the University of Chicago (NSF DMR-1420709).

## REFERENCES

- (1) Rogers, W. B.; Shih, W. M.; Manoharan, V. N. *Nat. Rev. Mater.* **2016**, *1* (3), 16008.
- (2) Walther, A.; Müller, A. H. E. *Chem. Rev.* **2013**, *113* (7), 5194–5261.
- (3) Lim, D.-K. K.; Jeon, K.-S. S.; Kim, H. M.; Nam, J.-M. M.; Suh, Y. D. *Nat. Mater.* **2010**, *9* (1), 60–67.
- (4) Lim, D.-K.; Jeon, K.-S.; Hwang, J.-H.; Kim, H.; Kwon, S.; Suh, Y. D.; Nam, J.-M. *Nat. Nanotechnol.* **2011**, *6* (7), 452–460.
- (5) Taylor, R. W.; Lee, T. C.; Scherman, O. A.; Esteban, R.; Aizpurua, J.; Huang, F. M.; Baumberg, J. J.; Mahajan, S. *ACS Nano* **2011**, *5* (5), 3878–3887.
- (6) Liu, X.; Biswas, S.; Jarrett, J. W.; Poutrina, E.; Urbas, A.; Knappenberger, K. L.; Vaia, R. A.; Nealey, P. F. *Adv. Mater.* **2015**, *27* (45), 7314–7319.
- (7) Biswas, S.; Liu, X.; Jarrett, J. W.; Brown, D.; Pustovit, V.; Urbas, A.; Knappenberger, K. L.; Nealey, P. F.; Vaia, R. A. *Nano Lett.* **2015**, *15* (3), 1836–1842.
- (8) Lin, Q.-Y.; Mason, J. A.; Li, Z.; Zhou, W.; O'Brien, M. N.; Brown, K. A.; Jones, M. R.; Butun, S.; Lee, B.; Dravid, V. P.; Aydin, K.; Mirkin, C. A. *Science* **2018**, *359* (6376), 669–672.
- (9) Hung, A. M.; Micheel, C. M.; Bozano, L. D.; Osterbur, L. W.; Wallraff, G. M.; Cha, J. N. *Nat. Nanotechnol.* **2010**, *5* (2), 121–126.
- (10) Flauraud, V.; Mastrangeli, M.; Bernasconi, G. D.; Butet, J.; Alexander, D. T. L. L.; Shahrabi, E.; Martin, O. J. F. F.; Brugger, J. *Nat. Nanotechnol.* **2017**, *12* (1), 73–80.
- (11) Hughes, R. A.; Menumerov, E.; Neretina, S. *Nanotechnology* **2017**, *28* (28), 282002.
- (12) Nordlander, P.; Oubre, C.; Prodan, E.; Li, K.; Stockman, M. I. *Nano Lett.* **2004**, *4* (5), 899–903.

- (13) Deng, T.-S.; Parker, J.; Yifat, Y.; Shepherd, N.; Scherer, N. F. *J. Phys. Chem. C* **2018**, *122* (48), 27662–27672.
- (14) Hao, E.; Schatz, G. C. *J. Chem. Phys.* **2004**, *120* (1), 357–366.
- (15) Dadosh, T.; Sperling, J.; Bryant, G. W.; Breslow, R.; Shegai, T.; Dyshel, M.; Haran, G.; Bar-Joseph, I. *ACS Nano* **2009**, *3* (7), 1988–1994.
- (16) Yin, H. J.; Liu, L.; Shi, C. A.; Zhang, X.; Lv, M. Y.; Zhao, Y. M.; Xu, H. J. *Appl. Phys. Lett.* **2015**, *107* (19), 193106.
- (17) Mirin, N. A.; Bao, K.; Nordlander, P. *J. Phys. Chem. A* **2009**, *113* (16), 4028–4034.
- (18) Yang, Z.-J.; Zhang, Z.-S.; Zhang, L.-H.; Li, Q.-Q.; Hao, Z.-H.; Wang, Q.-Q. *Opt. Lett.* **2011**, *36* (9), 1542–1544.
- (19) Wu, D.; Jiang, S.; Liu, X. *J. Phys. Chem. C* **2012**, *116* (25), 13745–13748.
- (20) Pakizeh, T.; Käll, M. *Nano Lett.* **2009**, *9* (6), 2343–2349.
- (21) Brown, L. V.; Sobhani, H.; Lassiter, J. B.; Nordlander, P.; Halas, N. J. *ACS Nano* **2010**, *4* (2), 819–832.
- (22) Zhang, X.; Servos, M. R.; Liu, J. *J. Am. Chem. Soc.* **2012**, *134* (17), 7266–7269.
- (23) Hurst, S. J.; Lytton-Jean, A. K. R. R.; Mirkin, C. A. *Anal. Chem.* **2006**, *78* (24), 8313–8318.
- (24) Halperin, A.; Buhot, A.; Zhulina, E. B. *Langmuir* **2006**, *22* (26), 11290–11304.
- (25) Romero, I.; Aizpurua, J.; Bryant, G. W.; Garcia de Abajo, F. J. *Opt. Express* **2006**, *14* (21), 9988.
- (26) Timmermans, F. J.; Lenferink, A. T. M.; Van Wolferen, H. A. G. M.; Otto, C. *Analyst* **2016**, *141* (23), 6455–6462.
- (27) Rechberger, W.; Hohenau, A.; Leitner, A.; Krenn, J. R.; Lamprecht, B.; Aussenegg, F. R. *Opt. Commun.* **2003**, *220* (1–3), 137–141.
- (28) Su, K.-H.; Wei, Q.-H.; Zhang, X.; Mock, J. J.; Smith, D. R.; Schultz, S. *Nano Lett.* **2003**, *3* (8), 1087–1090.
- (29) Samoc, A.; Miniewicz, A.; Samoc, M.; Grote, J. G. J. *J. Appl. Polym. Sci.* **2007**, *105* (1), 236–245.
- (30) Welch, B. L. *Biometrika* **1947**, *34* (1–2), 28–35.
- (31) Jain, P. K.; Huang, W.; El-Sayed, M. A. *Nano Lett.* **2007**, *7* (7), 2080–2088.
- (32) Xie, H.; Lin, Y.; Mazo, M.; Chiappini, C.; Sánchez-Iglesias, A.; Liz-Marzán, L. M.; Stevens, M. M. *Nanoscale* **2014**, *6* (21), 12403–12407.
- (33) Novara, C.; Chiadò, A.; Paccotti, N.; Catuogno, S.; Esposito, C. L.; Condorelli, G.; De Franciscis, V.; Geobaldo, F.; Rivolo, P.; Giorgis, F. *Faraday Discuss.* **2017**, *205*, 271–289.
- (34) Itoh, T.; Kikkawa, Y.; Yoshida, K.; Hashimoto, K.; Biju, V.; Ishikawa, M.; Ozaki, Y. *J. Photochem. Photobiol., A* **2006**, *183* (3), 322–328.
- (35) Zheng, Y.; Rosa, L.; Thai, T.; Ng, S. H.; Gómez, D. E.; Ohshima, H.; Bach, U. *J. Mater. Chem. A* **2015**, *3* (1), 240–249.
- (36) Hofmann, A.; Schmiel, P.; Stein, B.; Graf, C. *Langmuir* **2011**, *27* (24), 15165–15175.
- (37) Gandra, N.; Abbas, A.; Tian, L.; Singamaneni, S. *Nano Lett.* **2012**, *12* (5), 2645–2651.
- (38) Weller, L.; Thacker, V. V.; Herrmann, L. O.; Hemmig, E. A.; Lombardi, A.; Keyser, U. F.; Baumberg, J. J. *ACS Photonics* **2016**, *3* (9), 1589–1595.
- (39) Spackova, B.; Wrobel, P.; Bockova, M.; Homola, J. *Proc. IEEE* **2016**, *104* (12), 2380–2408.
- (40) Wang, Y.; MacLachlan, E.; Nguyen, B. K.; Fu, G.; Peng, C.; Chen, J. I. L. *Analyst* **2015**, *140* (4), 1140–1148.
- (41) Zhang, X.; Chen, Y. L.; Liu, R.-S.; Tsai, D. P. *Rep. Prog. Phys.* **2013**, *76* (4), 046401.
- (42) Robotjazi, H.; Bahauddin, S. M.; Doiron, C.; Thomann, I. *Nano Lett.* **2015**, *15* (9), 6155–6161.
- (43) Furube, A.; Du, L.; Hara, K.; Katoh, R.; Tachiya, M. *J. Am. Chem. Soc.* **2007**, *129* (48), 14852–14853.
- (44) Biswas, S.; Duan, J.; Nepal, D.; Park, K.; Pachter, R.; Vaia, R. A. *Nano Lett.* **2013**, *13* (12), 6287–6291.

## ■ NOTE ADDED AFTER ASAP PUBLICATION

This paper was published ASAP on June 18, 2019 with an error in the Results section. The corrected version was reposted on June 19, 2019.

**Supporting information for**

# **Hierarchical Assembly of Plasmonic Nanoparticle Heterodimer Arrays with Tunable Sub-5 nm Nanogaps**

*Jiajing Li<sup>†</sup>, Tian-Song Deng<sup>‡,§</sup>, Xiaoying Liu<sup>†</sup>, James A. Dolan<sup>†,||,⊥</sup>, Norbert F. Scherer<sup>‡,§</sup>, Paul F. Nealey<sup>†,||,⊥,\*</sup>*

<sup>†</sup> Pritzker School of Molecular Engineering, University of Chicago, Chicago, IL 60637, USA

<sup>‡</sup> The James Franck Institute, University of Chicago, Chicago, IL 60637, USA

<sup>§</sup> Department of Chemistry, University of Chicago, Chicago, IL 60637, USA

<sup>||</sup> Material Science Division, Argonne National Laboratory, Lemont, IL 60439, USA

<sup>⊥</sup> Pritzker School of Molecular Engineering, Argonne National Laboratory, Lemont, IL 60439,  
USA

## 1. Experimental section

**Fabrication of single AuNP arrays.** Silicon <100> wafers were purchased from WRS Materials, LLC. Cross-linkable polystyrene (PS) containing 4% glycidyl methacrylate as a crosslinking agent was synthesized as described previously<sup>1</sup>. Hydroxyl-terminated poly(ethylene glycol) methyl ethers (PEG-OH,  $M_n = 32000$  g/mol) was purchased from Polymer Source, Inc. Poly(methyl methacrylate) (PMMA) photoresist (950 kg/mol, 4 wt% in chlorobenzene) was purchased from MicroChem, Inc. AuNPs with citrate ligands were purchased from Ted Pella, Inc. 2-propanol (IPA), 4-methyl-2-pentanone (MIBK), chlorobenzene and 1-methyl-2-pyrrolidinone (NMP) were purchased from Aldrich and used as received.

Substrates were spin-coated from a 0.5 wt% solution of cross-linkable PS in toluene, followed by annealing at 190°C under vacuum for 24 hours to form the crosslinked PS (xPS) mat. Diluted PMMA photoresist (1.5 wt% in chlorobenzene) was then spin-coated on top, and electron beam lithography was performed to create desired dot arrays. After resist development with a mixture of MIBK and IPA (1:3 by volume), the patterned substrates were exposed to oxygen plasma (20 W, 30 s) to remove xPS in the patterned areas. The exposed areas were then functionalized with PEG-OH by spin coating from a 1.5 wt% solution in chlorobenzene and annealing at 200°C for 5 min in a nitrogen atmosphere. The remaining photoresist and excess PEG-OH were removed by sonication in NMP (3 min, 2 cycles) and chlorobenzene (3 min, 1 cycle). For adsorption of AuNPs onto patterned areas, 100  $\mu$ L AuNP suspension was deposited on the substrate and left still for 40 min in a humid environment. The substrates were then rinsed thoroughly with water and dried with nitrogen.

**Synthesis of AuNP-DNA conjugates.** NAP-5 columns were purchased from GE Healthcare, Inc. 1,4-dithiothreitol (DTT), sodium chloride (NaCl), sodium dodecyl sulfate (SDS), sodium phosphate monobasic and sodium phosphate dibasic were purchased from Aldrich and used as received. All oligonucleotides were purchased from Integrated DNA Technologies, Inc and are sequenced as follows:

ssDNA1: TAA CAA TAA TCC CTC TTT TTT TTT T-SH

(Cy5-TAA CAA TAA TCC CTC TTT TTT TTT T-SH for Raman scattering measurement)

ssDNA2: GAG GGA TTA TTG TTA TTT TTT TTT T-SH

ssDNA3: SH-T TTT TTT TTT TAC TTT TCA AGT ACT CTG TGA

linker DNA: GAG GGA TTA TTG TTA TCA CAG AGT ACT TGA AAA GTA

AuNP-DNA conjugates were synthesized following a thiol-assisted attachment process as reported previously<sup>2,3</sup>. Briefly, ssDNA2 (or ssDNA3) was treated with 0.1 M DTT solution (pH = 8) for 1 hour and desalted using NAP-5 columns. The purified oligonucleotides were mixed with AuNPs solution (approximately 3000 oligonucleotides/AuNP) and mixed for 1 h on a mixer to form an initial loose loading. The surfactant SDS was then added to the mixture to bring the final concentration of SDS to 0.1%, followed by the addition of 500 mM citrate buffer (pH = 3). After bringing the concentration of citrate buffer to 10 mM, the mixture was placed on a mixer for 2 h for further DNA loading. For a “salt aging” process, 2M NaCl solution was slowly added to the mixture over the next 1 h to bring the final concentration of NaCl to 0.3 M and the solution was allowed to mix for another 2 h. The excess oligonucleotides were removed by three rounds of centrifugation (7000 rpm, 15 min each) and the AuNP-DNA conjugates were resuspended in hybridization buffer (0.3 M NaCl, 0.1% SDS, 0.01 M phosphate buffer, pH = 7).

**Fabrication of heterodimer arrays.** Arrays of single AuNPs were functionalized with ssDNA1 following a similar procedure as used to synthesize AuNP-DNA conjugates. After treatment with DTT and desalting, purified ssDNA1 was dissolved in a solution of 1 M NaCl, 0.1% SDS and 0.01 M phosphate buffer (pH = 7). The final concentration of oligonucleotides was 2  $\mu$ M. Substrates were functionalized with single AuNP arrays by soaking in the ssDNA1 solution and being placed on a mixer overnight to complete the DNA loading. After loading is complete, substrates were rinsed by 0.3 M NaCl, 0.1% SDS and distilled water, respectively, and dried with nitrogen. For “15 bps” dimers, the substrates were soaked in solution of AuNP-ssDNA2 conjugates in hybridization buffer (0.3M NaCl, 0.1% SDS, 0.01M phosphate buffer, pH = 7) and placed on a mixer overnight. Following hybridization, the substrates were rinsed with 0.3 M NaCl, 0.1% SDS and distilled water, followed by drying with nitrogen. For “36 bps” dimers, the substrates were first soaked in solution of 2  $\mu$ M linker DNA in hybridization buffer and mixed for 7 hours to complete hybridization. After rinsing with 0.3 M NaCl, 0.1% SDS and distilled water, the substrates hybridized with AuNP-ssDNA3 conjugates. The assembled structures were imaged by a high-resolution Field-Emission Scanning Electron Microscope (Carl Zeiss Merlin).

**Scattering Spectroscopy.** Samples were prepared on indium tin oxide (ITO)-coated glass substrates (Structure Probe, Inc) and scattering spectra were measured using a home-built set-up. Prior to scattering measurements, samples were imaged with SEM to determine the direction of the dimer axis. The SEM images were taken at relatively low magnification (15,000 $\times$ ) and short dwell time (6  $\mu$ s) in a single frame to minimize any potential effect of SEM imaging on the sample. The scattering setup is equipped with a linear polarizer, and the samples were rotated to align the measured dimer axis with the polarization axis of the incident light. A schematic of the set-up for single particle spectroscopy and microscopy is shown in Fig. S1. A broadband white light source

(Fianium, White Lase SC400, 400-2700 nm) was coupled to an inverted optical microscope equipped with an oil immersion objective with numerical aperture  $NA = 1.4$  (Olympus, IX-81; SAPO 100 $\times$ ). The back-scattered images of the sample plane were recorded by a sCMOS array detector (Andor Neo) connected to the eye-piece of the trinocular microscope, and spectra were acquired by an EM-CCD (Andor Newton) connected to an imaging spectrometer (Andor Shamrock 193i) coupled to the side port of the microscope. To minimize the scattering from the coverslip and sample interface, a drop of immersion oil was put on the coverslip, and the inverted sample was placed on top of the immersion oil. Then the coverslip was put on the microscope for measurement. Background correction and normalization were performed for all measurements.

**Raman Scattering.** Raman spectra were collected on a Horiba LabRAM HR Evolution Raman spectrometer (Horiba, Ltd.) with 633 nm HeNe laser (77.5  $\mu$ W) and 100 $\times$  objective. The Raman spectra were recorded in the range of 800–1800  $\text{cm}^{-1}$  with 1 s acquisition, 2 accumulations. All data were baseline-corrected by subtracting the background spectra.

**Numerical Simulations.** FDTD calculations were conducted using FDTD Solutions (Lumerical Solutions, Inc.) software. The simulation set-up is shown in Fig. S2. The environmental refractive index was set as 1.5, corresponding to that of the immersion oil. Gold was simulated using a complex refractive index from Palik et al.<sup>4</sup> and a previously reported model<sup>5</sup> was employed to describe the optical properties of ITO. XPS, PEG brush, and glass were simulated as dielectric materials with real dielectric constants. The spectra were recorded by a frequency-domain field monitor. For simulation of SERS, 633 nm incident light was used instead of broadband white light and the environmental refractive index was set to 1.0 corresponding to that of air.

## 2. Disentangling the impact of particle size and gap size on distribution of longitudinal plasmon peak positions

A series of simulations were conducted to calculate the longitudinal plasmon resonances of the heterodimers at various gap sizes (from 2 nm to 7 nm) for different size of dimers (from 114 nm to 146 nm). The peak position is approximately linear with gap size and dimer size in the range of calculations:

$$P = a_0 + a_1G + a_2R, \quad (1)$$

where  $P$  is the peak position in nm,  $G$  is the gap size in nm, and  $R$  is the size (diameter) of the dimer along the major axis. The variables  $a_0$ ,  $a_1$  and  $a_2$  are fitting parameters. The adjusted  $R^2$  value of the fitted curve is 0.9522, corresponding to  $a_0 = 581.3$ ,  $a_1 = -8.074$ , and  $a_2 = 0.9081$ . Based on equation (1) and the error propagation rules<sup>6</sup>, the standard deviation of the peak position may be calculated as

$$\sigma^2(P) = a_1^2\sigma^2(G) + a_2^2\sigma^2(R), \quad (2)$$

where  $\sigma(G)$  is the standard deviation of the gap size and  $\sigma(R)$  is the standard deviation of the dimer diameter.

Since  $R = R_1 + R_2$ , where  $R_1 = 80$  nm,  $R_2 = 50$  nm, and the relative standard deviation of particle size is 8% for both 80 nm and 50 nm AuNPs, as provided by manufacturer,  $\sigma^2(R)$  is

$$\sigma^2(R) = \sigma^2(R_1) + \sigma^2(R_2) = (80 \times 0.08)^2 + (50 \times 0.08)^2 = 57 \text{ (nm}^2\text{)}. \quad (3)$$

Since  $\sigma^2(P)$  is measured experimentally,  $\sigma(G)$  is the only unknown variable in equation (2). We can therefore estimate the standard deviation of gap size  $\sigma(G)$  to be 1.0 nm for “15” bps dimers and 0.8 nm for “36 bps” dimers.

Note that the impact of particle shape variation is not included in this calculation, which would contribute another term to (1) and (2), and lead to an even smaller estimate of deviation of gap size.

### 3. Supplementary figures

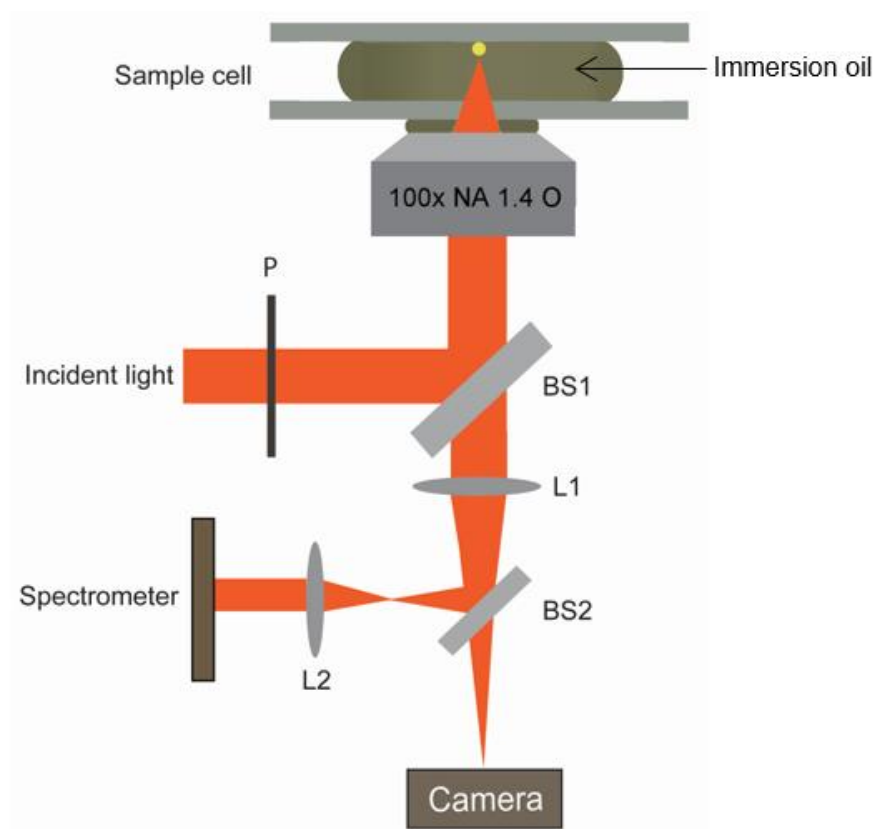


**Figure S1.** Home built setup for single-particle far-field scattering measurements. P: polarizer, BS: beam splitter, L: lens. A spatially coherent (broadband) white light continuum is coupled to an inverted optical microscope equipped with an oil immersion objective (100 $\times$ ) with numerical aperture,  $NA \leq 1.4$ . The backscattered images and spectra of the sample plane are recorded either by a CCD array detector connected to the eyepiece of the microscope or by a CCD connected to an imaging spectrometer. Note that not all lenses and optical components are shown for simplicity.

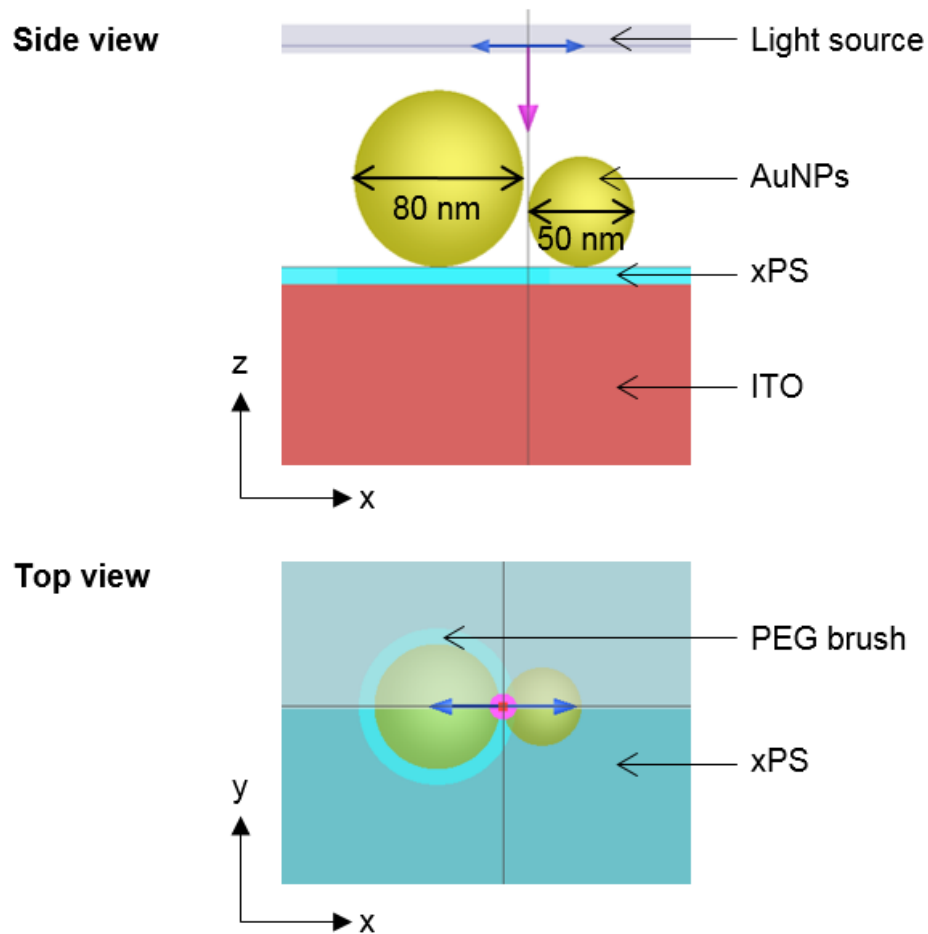


**Figure S2.** Side view and top view of FDTD simulation. Simulation replicates the experimental configuration. Dielectric functions: Au (Palik<sup>4</sup>), ITO (Konig<sup>5</sup>), xPS (refractive index  $n=1.59^7$ ), PEG brush ( $n=1.46$ ), immersion medium ( $n=1.5$ ). Dimensions ( $t$ =thickness,  $d$ =diameter):  $t_{\text{ITO}}=105$  nm,  $t_{\text{xPS}}=8$  nm,  $t_{\text{PEG}}=8$  nm,  $d_{\text{PEG}}=100$  nm. Incident light is polarized along the x axis and spectra are recorded by the frequency-domain field monitor (not shown). Symmetric boundary condition has been chosen for efficiency.

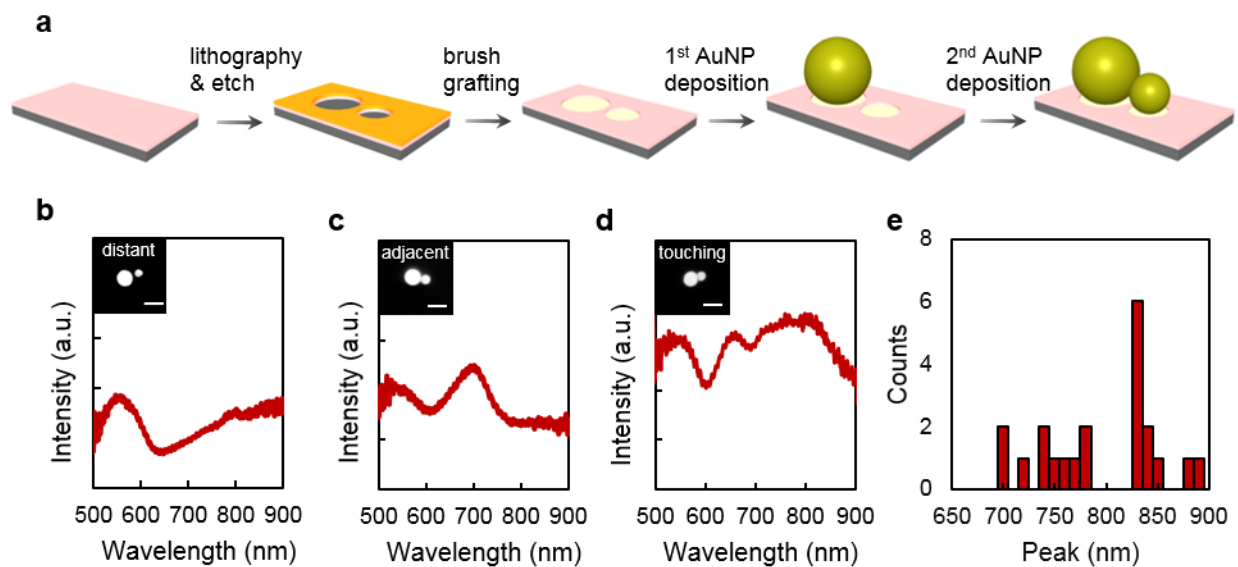


**Figure S3.** Fabrication of 80-50 nm heterodimers without DNA and the corresponding scattering spectra. (a) Schematic of the process for positioning and patterning AuNPs into heterodimers on chemically patterned substrates without DNA. The assembly solely depends on template-particle interactions and the two AuNPs can be (b) distant from, (c) adjacent to or (d) touching each other, giving rise to one, two or three peaks respectively. (e) A broad distribution of rightmost peak positions indicates that the gaps are much less controlled using this approach compared with hierarchical assembly with DNA included.

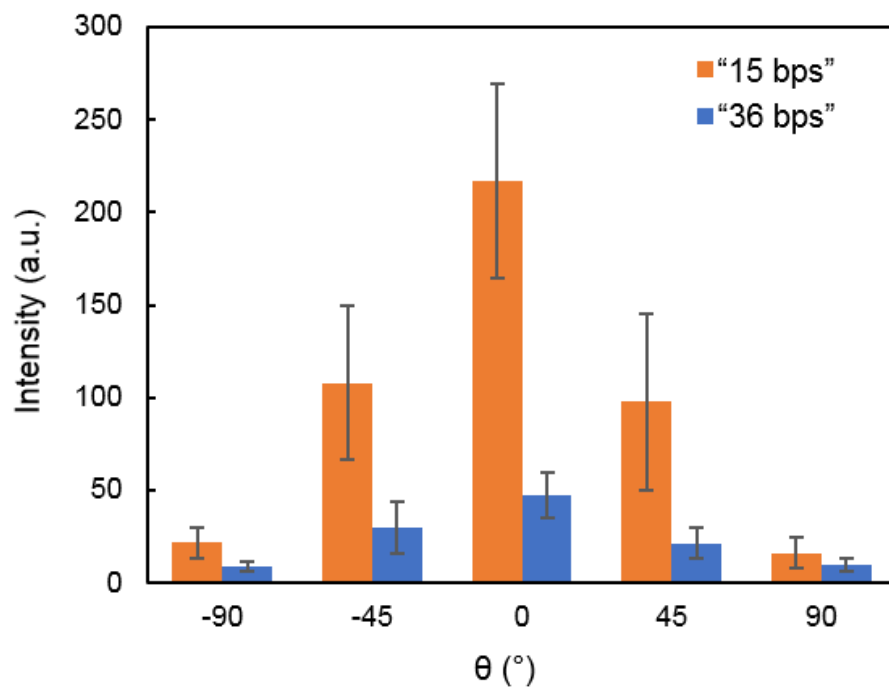


**Figure S4.** Polarization-dependent SERS intensities at  $1589\text{ cm}^{-1}$ . “15 bps” dimers show stronger SERS enhancement than that from “36 bps” dimers due to the associated smaller gap of the heterodimers. Intensities are averaged from five heterodimers for the two types of dimers respectively, and error bars represent one standard deviation.

## References

- (1) Onses, M. S.; Nealey, P. F. *Small* **2013**, 9 (24), 4168–4174.
- (2) Zhang, X.; Servos, M. R.; Liu, J. *J. Am. Chem. Soc.* **2012**, 134 (17), 7266–7269.
- (3) Hurst, S. J.; Lytton-Jean, A. K. R. R.; Mirkin, C. A. *Anal. Chem.* **2006**, 78 (24), 8313–8318.
- (4) Palik, E. *Handbook of Optical Constants of Solids*; Elsevier, **1997**.
- (5) Konig, T. A. F.; Ledin, P. A.; Kerszulis, J.; Mahmoud, M. A.; El-Sayed, M. A.; Reynolds, J. R.; Tsukruk, V. V. *ACS Nano* **2014**, 8 (6), 6182–6192.
- (6) Taylor, J. R. *An Introduction to Error Analysis*; University Science Books: Sausalito, CA, **1996**.
- (7) Sultanova, N.; Kasarova, S.; Nikolov, I. *Acta Phys. Pol. A* **2009**, 116 (4), 585–587.